# 5. FE Evaluation of Contact-Impact Forces

## 5.1. Introduction

This chapter reports numerical examples of wheel/rail contact impact at IRJs obtained using the FE model described in the previous chapter. The results of the examples are presented as the wheel-rail contact force time histories. The contact patch parameters, the peak contact pressure and the contact distribution away from and close to the end post are also discussed; where possible comparisons are made with Hertzian contact theory. The effects of some selected IRJ design parameters to the magnitude of the impact force are studied through several sensitivity analyses.

## 5.2. Numerical Example: Typical Input Data

All simulations are run on the Altix 3700 BX2 super computer installed at the Australian Partnership for Advanced Computing (APAC), Canberra. The system contained CPU type Itanium2 (1.6GHz) and the maximum memory allowance for each run has been 4069Mb. Typical computational time for the combined static and dynamic analysis was 35 hours, of which the dynamic analysis took 28 hours.

A wheel with a vertical load of 150KN (corresponding to gross wagon mass of 120 tonnes) was assumed to travel at a speed of 120km/h over the IRJ. Although most freight wagons and all coal wagons run at a maximum spend of 80 km/h, a higher speed (120km/h) was adopted to reduce the duration of travel for simulating the

required travelling length of 400mm. The example with a lower speed (<80km/h) corresponding to the field test is reported in Chapter 7.

Fig. 5.1 shows the load and boundary conditions used in the static analysis. The bolt pretension load of 200KN corresponding to the torque of 1050Nm was applied to the bolt shank and the wheel load of 150KN was applied vertically downwards at the axis of the wheel (identified as B in Fig. 5.1). In the static analysis, the wheel/rail contact position was located at 218mm away from the IRJ centre (shown in Fig. 5.1).

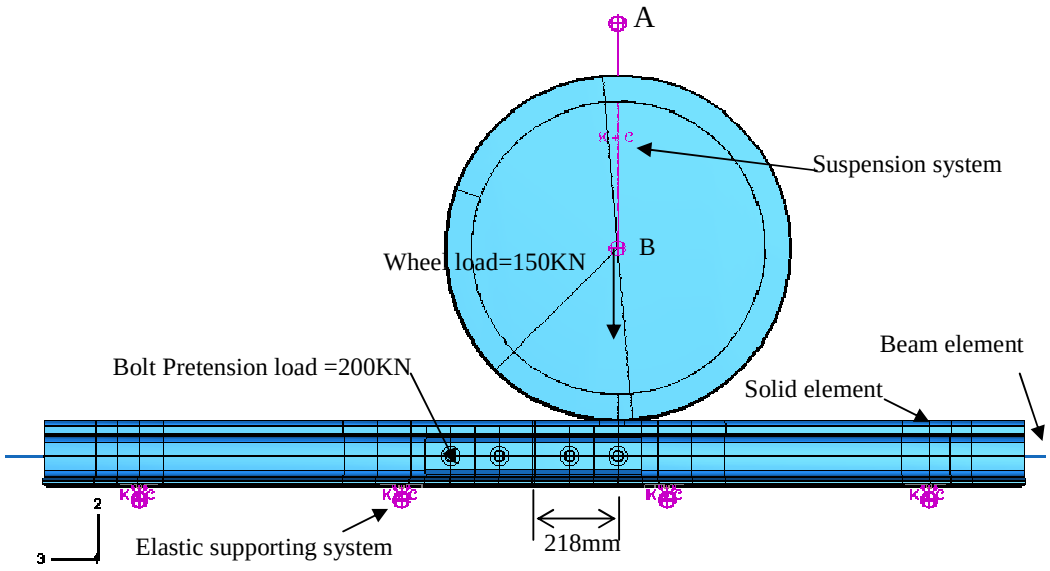


Figure 5.1 Typical wheel/rail static contact model of IRJ

For the purpose of smooth transfer of static analysis results into dynamic analysis input data, it was required to apply the centrifugal force (see Fig. 4.23) due to the steady state velocity of the wheel in the static analysis. This was achieved by prescribing the velocity at Point B in ABAQUS/CAE. The mass of the wagon shared by the wheel was also applied (at point A in Fig. 5.1) to enable smooth transfer of the

static results into the dynamic analysis input data.

In the dynamic analysis, the model was preloaded by transferring the results from the static analysis. The longitudinal speed 120km/h and the rotational angular speed 72.46 rad/s were applied to the wheel as the initial conditions. A similar approach is also adopted for the simulation of automobile tyre-road interaction problems (ABAQUS, 2003). Initial condition instabilities were minimised by allowing the wheel to roll a sufficiently long distance (218mm) prior to impacting the IRJ. The total duration of this simulation in real time was 12ms.

The mechanical properties of the material are shown in Table 5.1. In this example, the end post thickness was kept as10mm and the end post material was assumed glued to the rail ends for simplicity. The suspension system and the elastic supporting system were modelled as spring/dashpot sets, and their mechanical properties are shown in Table 5.2.

Table 5.1 Mechanical properties of steel and insulation material (Chen, 2002)

| *Property* | *Steel* | *Nylon66* |
|---|---|---|
| Young's modulus | 210GPa | 1.59GPa |
| Poisson's ratio | 0.3 | 0.39 |
| Density | 7800kg/$m^3$ | 1140kg/$m^3$ |
| Yield Stress | 780MPa | _ |

Table 5.2 Properties of the Supporting and Suspension system (Wen, 2005)

| Elastic support system | Suspension system |
|---|---|
| Stiffness $K_b$ (MN/m) 26.8 | Stiffness $K_s$ (KN/m) 220 |
| Damping $C_b$ (KNs/m) 14.5 | Damping $C_s$ (Ns/m) 138 |

## 5.3. Typical Results

In this section, typical results of static and dynamic analysis are presented. The static results are presented first; the contact impact force obtained from the dynamic analysis is presented later.

The results are presented with two main objectives; first to provide some confidence that the results are indeed plausible, and second to ensure that an engineering interpretation of the results is possible. In order to demonstrate the plausibility of the results, fine meshes were used, especially in the static analysis. Unfortunately these fine meshes could not be adopted for the complete analysis, especially for the dynamic explicit analyses, due to the limitation of the super computing facilities provided for the project. It should be remembered that the dynamic solution could only be obtained after 28 hours of computer CPU time with coarse mesh. Therefore, even with larger resources, fine meshes would not have been economically viable.

### 5.3.1. Results of static analysis

First the contact pressure contour obtained from the elastic and the elasto-plastic analyses are presented and compared with the HCT as shown in Fig. 5.2. The dashed ellipse represents the HCT contact patch. Table 5.3 presents the dimensions of the major and minor axes of contact areas, as well as the contact area ($\pi ab$) and the peak pressure obtained from the elastic and elasto-plastic FE analyses and that of the HCT.

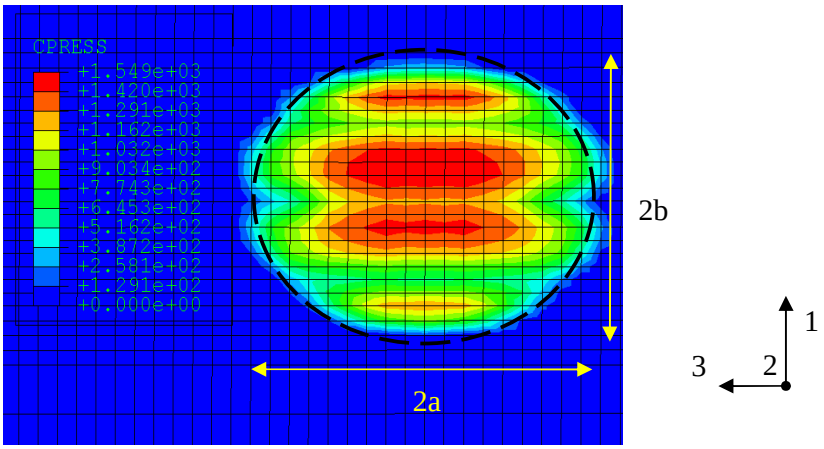


(a) Elastic FEA

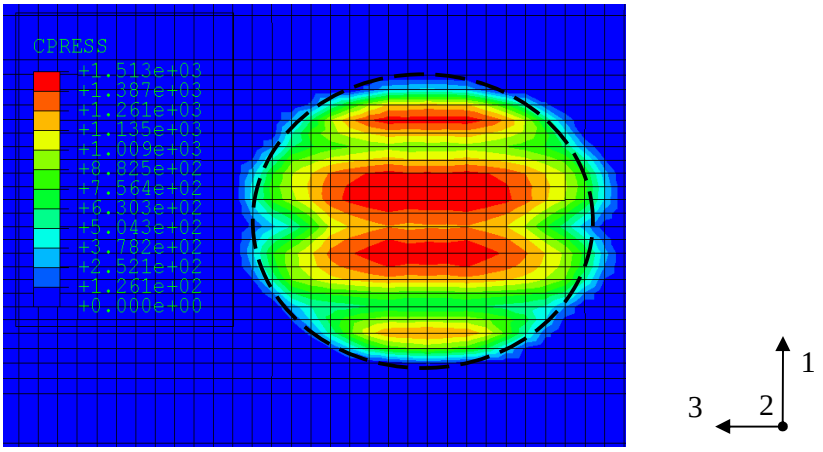


(b) Elasto-plastic FEA

Figure 5.2 Contact pressure distributions

Table 5.3 HCT and FEA comparison

| | HCT | Elastic FE | | Elasto-platic FE | |
|---|---|---|---|---|---|
| | Values | Values | % Diff. | Values | % Diff. |
| Major axis $a$ | $7.9\,mm$ | $8.5\,mm$ | 7.6% | $8.5\,mm$ | 7.6% |
| Minor axis $b$ | $6.3\,mm$ | $6.0\,mm$ | 4.7% | $6.0\,mm$ | 4.7% |
| Contact area A | $157\,mm^2$ | $161\,mm^2$ | 2.5% | $162\,mm^2$ | 3.2% |
| Peak pressure $P_0$ | 1434MPa | 1549MPa | 8.0% | 1513MPa | 5.5% |

It is notable that all parameters of the contact patch obtained from the elastic and elasto-plastic analyses compare well with that of the HCT. Further refining of the mesh would have reduced the percentage difference between the FE results and the HCT predictions. However such attempts were not carried out as even the mesh shown in Fig. 5.2 had to be made coarser for the dynamic analyses for reasons explained earlier.

One interesting observation is that the FE analyses have predicted slightly larger contact areas as well as higher contact pressures. Indeed both methods must satisfy static equilibrium for the applied wheel load of 150 KN. To examine the matter further, the HCT and FE pressure distributions are compared in Fig. 5.3. From the non-continuous distribution of the contact pressure predicted by the FE (especially along the minor axis), the reason for higher peak contact pressure becomes obvious. It should also be realised that the HCT is an overly idealised theory and hence its prediction of smooth, continuous distribution of pressure should be treated carefully. As an idealised theory, the HCT pressure distribution could be regarded as ‘average’ from Fig. 5.3.

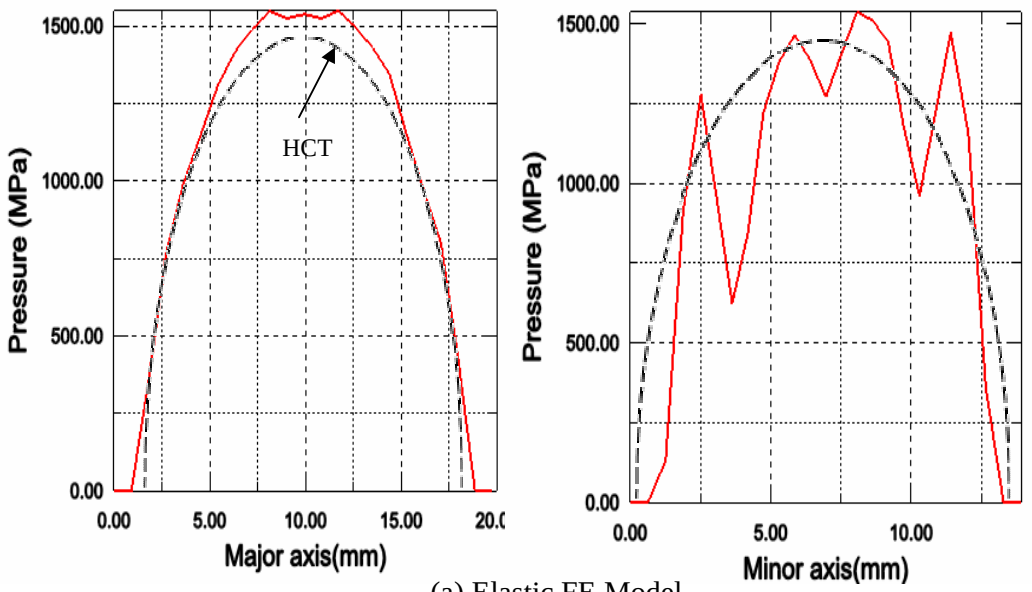


(a) Elastic FE Model

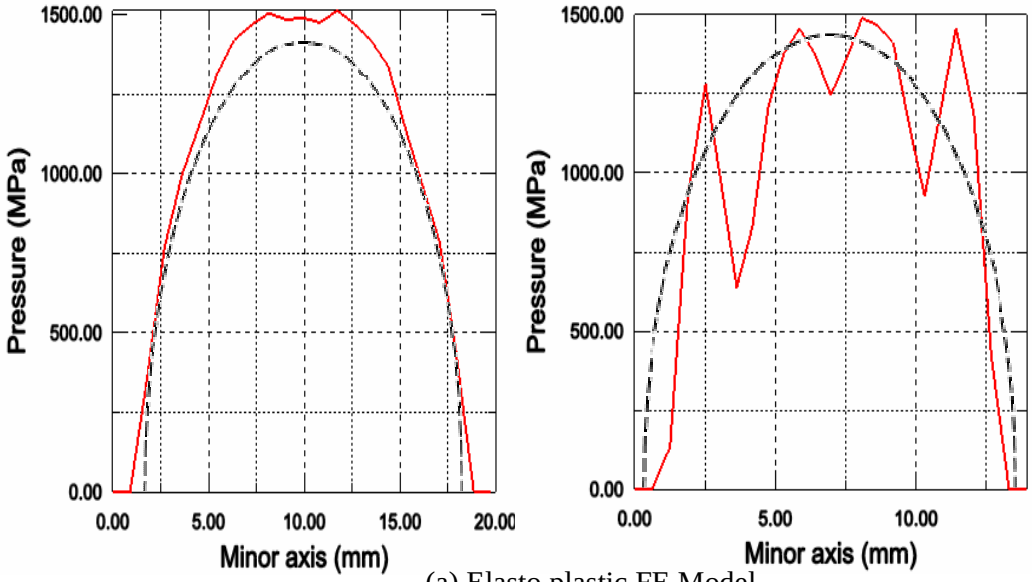


(a) Elasto plastic FE Model

Figure 5.3 Contact pressure distribution X-Y plot

Another observation to make is the effect of plasticity to peak pressure; only a marginal reduction in peak pressure has occurred due to the load of 150KN being just

sufficient to initiate the plastic deformation as shown in Fig. 5.4. Higher loads would have caused reduced pressure with the corresponding enlargement of contact area. Such analyses were not carried out as the main objective of the FE model was limited to the determination of the contact impact forces in the vicinity of the end post. The reason for the elaborate discussion of the contact patch is primarily to demonstrate that the FE contact model is appropriate.

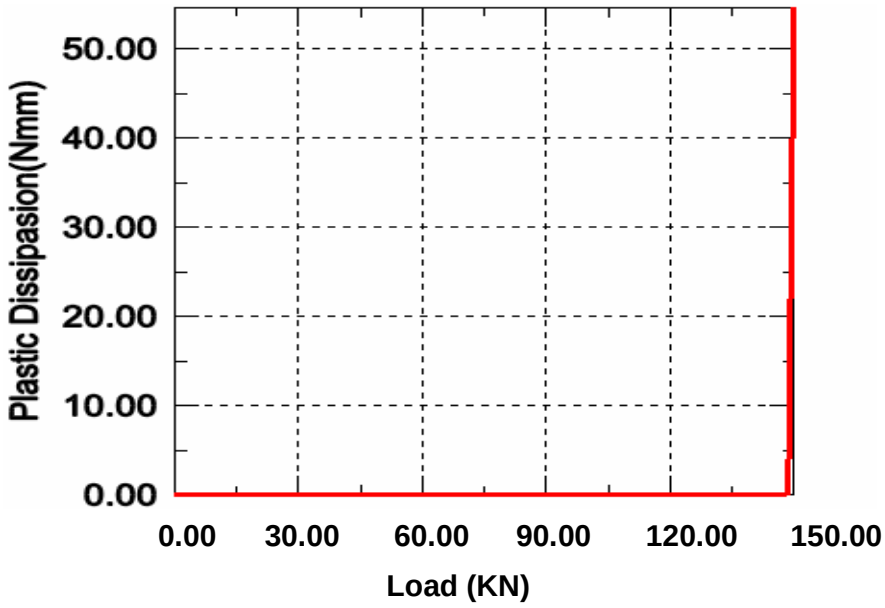


Fig 5.4 Plastic energy history

Unfortunately, as described above due to computational resource limitations, the mesh that has provided good static results (from the contact patch perspective) is not affordable in the dynamic analysis. In order to run the dynamic model within the constraints of available resources, the mesh was made coarser. The refined mesh used in the above two cases and the coarser mesh adopted for further analyses in the contact zones are shown in Fig. 5.5. It shows that the element size is enlarged by four times in the longitudinal direction (along axis 3) while in the radial and vertical

directions the element size has been kept unaltered.

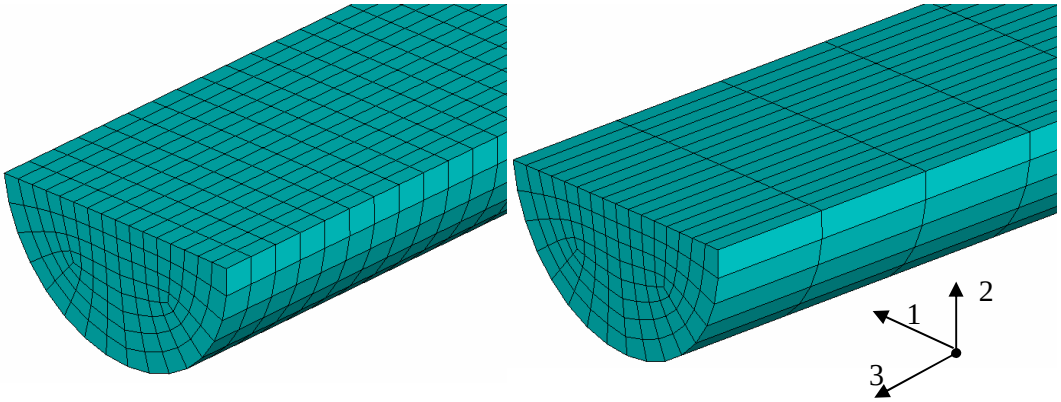


(a) Refined Mesh $0.9\text{mm}\times0.5\text{mm}\times0.5\text{mm}$ (b) Relaxed Mesh $3.6\text{mm}\times0.5\text{mm}\times0.5\text{mm}$

Figure 5.5 Mesh in the contact zone

The contact pressure distribution was obviously altered due to the coarser mesh as presented in Fig. 5.6. The analysis considered elasto-plastic rail steel properties. It indicates that due to the coarser mesh the contact area is enlarged by 17.3% ((190-162)/162) and the peak pressure is reduced by 10.6%((1513-1352)/1513). However, the results reported in the next section on dynamic analysis shows that the contact force and peak pressure are still sufficiently accurate.

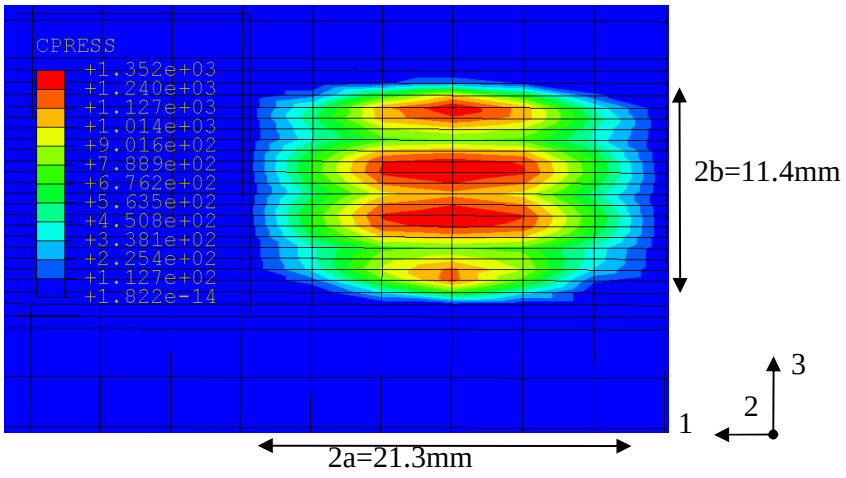


Figure 5.6 Contact pressure distribution of coarse mesh

### 5.3.2. Results of dynamic analysis

ABAQUS/Explicit permits two methods for contact constraint enforcement: the Penalty method and the Kinematic method. The effectiveness of these two methods was first examined. Fig. 5.7 indicates that both methods produce the same magnitude of the impact force, 174KN. However, the contact force history due to the Kinematic method has exhibited more severe vibration than that due to the Penalty method. This might have been associated with the algorithm of the Kinematic method that advances the kinematic state of the model into a predicted configuration *without considering the contact conditions*. The computational times of these two methods are fairly similar. The Kinematic method is therefore not chosen for further analyses because of its severe numerical vibration; all calculations carried out and results reported in this thesis were based on the Penalty method.

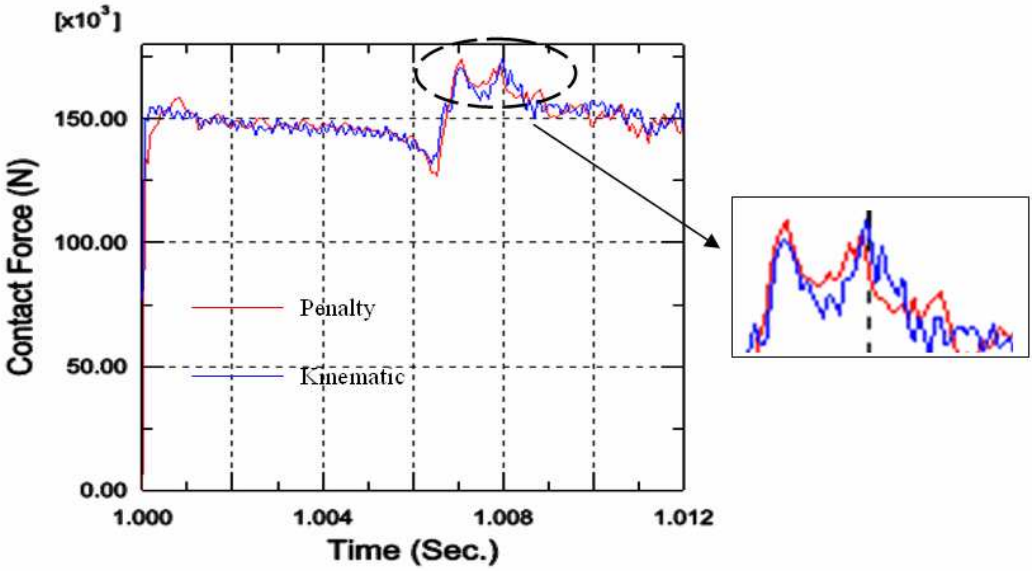


Figure 5.7 Contact force history using Penalty method and Kinematic method

**(a) Contact forces**

Dynamic analysis of the IRJ has provided the railhead/wheel contact force time history, which is shown in Fig.5.8.

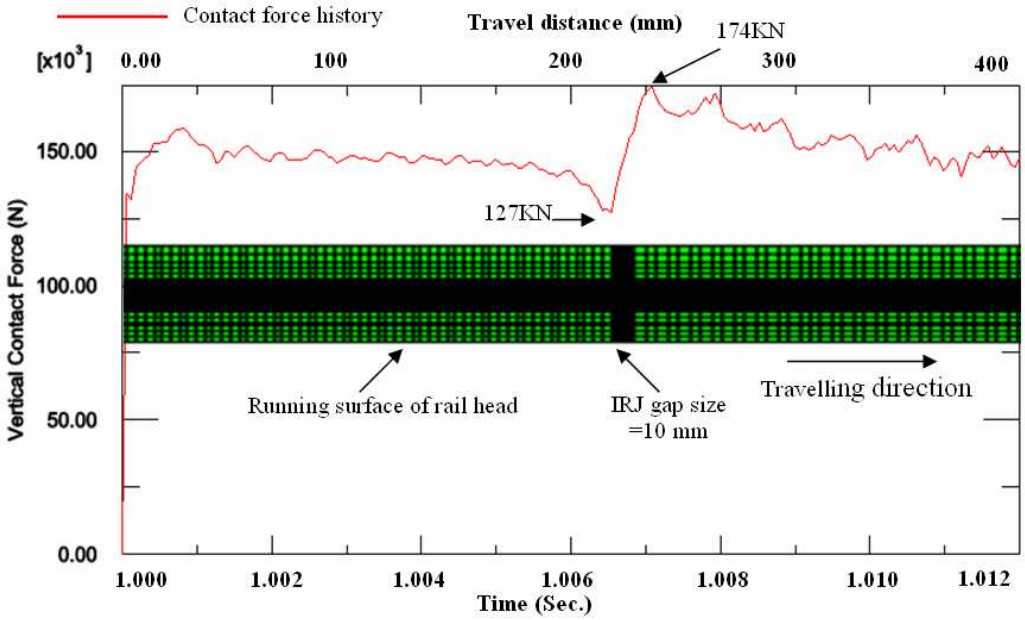


Figure 5.8 Rail/wheel contact force history

Fig.5.8 shows that, at the beginning of the dynamic analysis, the contact force has increased sharply just above 150KN and stabilised to the static wheel load value of 150kN after a short period of approximately 1.2 milliseconds. As the wheel approached the end post, a drop in the contact force (127kN) occurred due to the local deformation of the edge of the railhead that is affected by the difference in the material properties between the two interacting materials (rail steel and endpost Nylon). Within 0.54 millisecond the contact force increased from 127kN to 174kN (or 37%) indicating the occurrence of the rail/wheel contact-impact. The impact occurred at 7.1 millisecond since the start of the wheel travel with the corresponding impact factor of 1.16 (calculated from the quotient of impact force on static load (1+(174-

150)/150)). The concept of wheel/IRJ contact impact is described previously in Chapter 2 Section 2.6 (See Fig. 2.14).

It is believed that the wheel impact at the rail edge is due to the momentary "loss" of contact leading to wheel flight across the end post with the wheel landing on the edge of the other railhead. The exact location of the wheel tending to lose contact and re-landing on the railhead can not be precisely estimated from the FE model. As 0.54 millisecond of "flight time" of the wheel travelling at 120km/h corresponds to 18.0mm which is larger than the end post (10mm gap) thickness, it is inferred that the hypothesis of wheel impact in the vicinity of the end post is approximately validated. After the impact, the contact force has gradually damped down to the static wheel load level of 150 KN. It should also be observed from Fig. 5.8 that the post impact history is associated with high frequency noise, which was relatively calm in the pre-impact stage. This again reinforces that the wheel has actually caused impact at the forward section of the railhead.

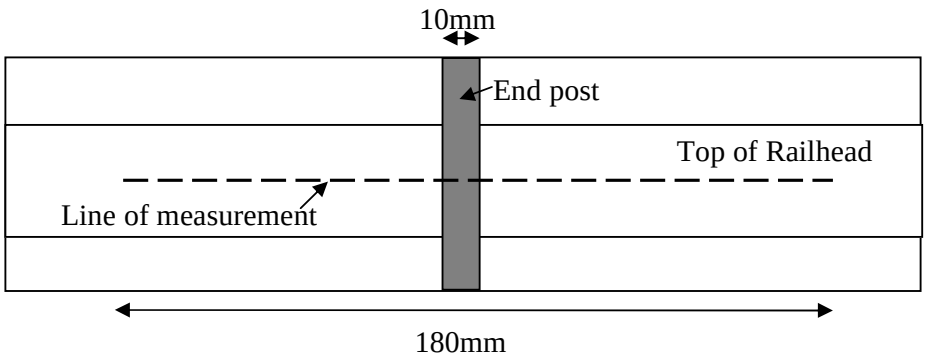

Figure 5.9 Measurement line on the top of railhead

The inferences discussed above can be further proven with the displacement profile of the IRJ as the wheel passing over the joint. The line of measurement is selected

through the nodes at the top centre line of railhead surface as shown in Fig. 5.9. The displacement of the selected nodes on this line is shown in Fig. 5.10.

Fig. 5.10 demonstrates that during pre-impact, Rail 1 has a lower profile than Rail 2 as the wheel load is primarily distributed on Rail 1. It shows that the end post was severely compressed by the uneven forces from the two rails which leads to a pop-up zone close to Rail 2. Because of the higher profile of Rail 2, the approaching wheel would hit Rail 2 severely at the edge of Rail 2 which is considered as an impact. At the moment of impact, the end post material under wheel contact loading dipped down significantly more than the two rail ends due to lower modulus. This deformed profile illustrates that only two point contact of the 460mm radius wheel in the vicinity of the end post as hypothysed in Section 2.6 would be possible. During the post impact stage, the deformation profile appears mirror-imaged to that of the pre impact behaviour.

**(b) Contact pressures and dimensions**

Contact pressure distribution at the top of the railhead obtained during one of the increments of the rolling of the wheel, corresponding to the pre-impact stage, is shown in Fig. 5.11. The shape of the contact pressure zone appears approximately elliptical with the major axis oriented along the longitudinal direction (shown by the single headed arrow) of travel. The dimension of the contact ellipse (a=10.35mm, b=6.35mm) is close to the static analysis using coarse mesh (see Fig. 5.6 in which a=10.65mm and b=5.70mm).

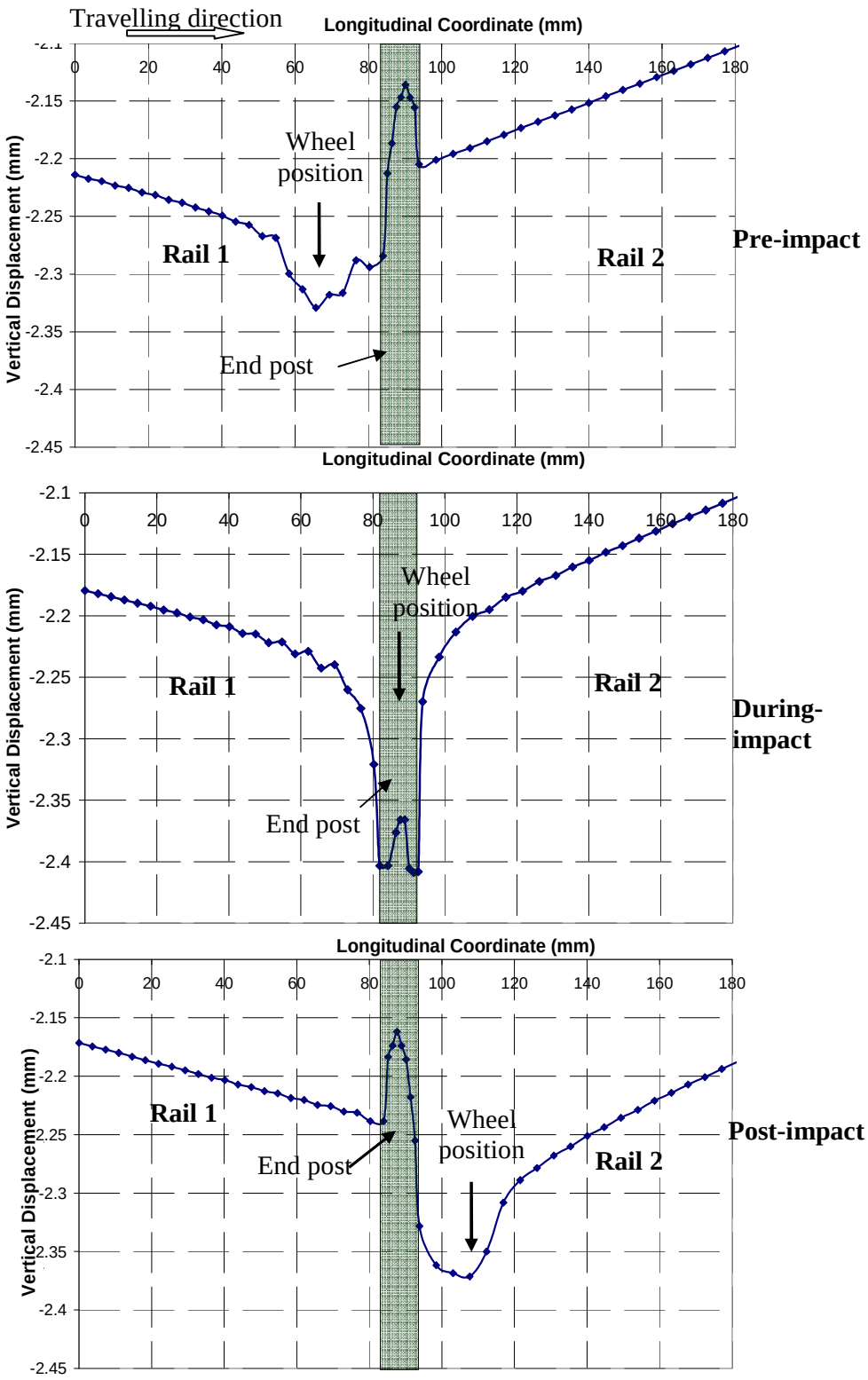


Figure 5.10 IRJ vertical displacement with wheel passing over the joint gap

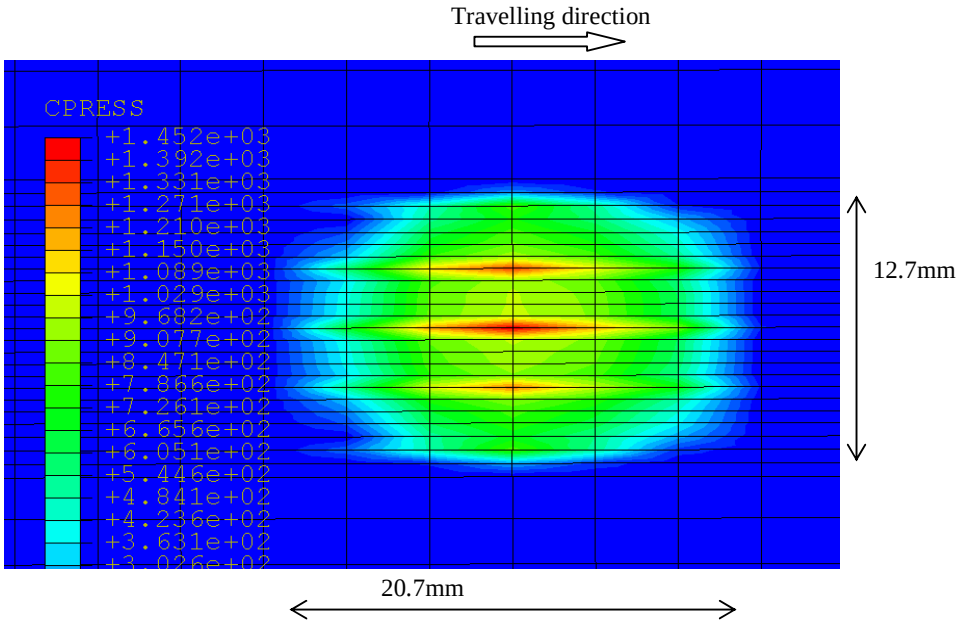


Figure 5.11 Contact pressure distribution (pre impact)

The peak pressures of the dynamic and static analyses obtained from the coarse mesh are 1352MPa and 1452MPa respectively. It is apparent that the dynamic rolling of the wheel has narrowed the peak pressure zone (compare the red contours of Fig. 5.11 and Fig. 5.6) with the corresponding increase in the peak pressure. As peak pressure is perhaps the most important parameter that affects the damage, its determination using dynamic analysis appears more appropriate, as this is likely to provide a less conservative estimation of the damage.

The contact pressure on the railhead was monitored throughout the travel of the wheel. Until the wheel approached the edge of the IRJ (closer to the end post), the contact pressure shape remained approximately elliptic. When the wheel just crossed the IRJ, the shape of the contact pressure distribution has shown two point contact of the

wheel spanning across the IRJ as illustrated in Fig. 5.12. The maximum contact pressure in this case was 1231MPa.

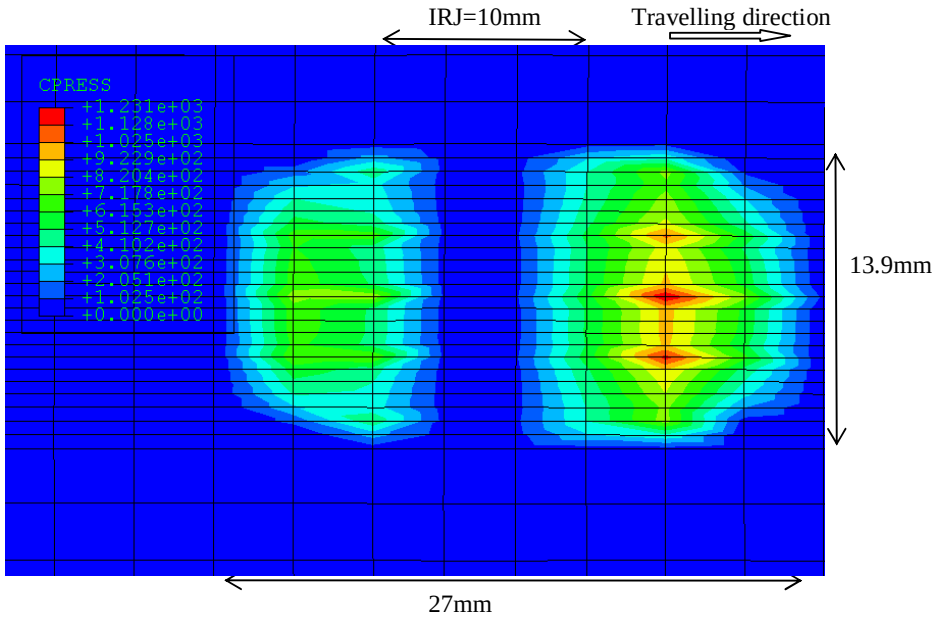


Figure 5.12 Contact pressure distribution (during impact)

Fig. 5.12 shows that the contact area was divided into two parts and the middle part corresponding to the end post was considered out of contact. In this situation, the continuous contact surface assumption of HCT was violated. This figure together with Fig. 5.10 infer that, at the time of impact, the wheel and rail are under a condition of 'two-point contact' in contrast with the 'single-point contact' beyond the vicinity of the end post. The post-impact contact pressure distribution on the railhead is shown in Fig. 5.13. It indicates the peak pressure of 1495MPa and the elliptical dimensions of major and minor axis are close that of the case just prior to impact as shown in Fig. 5.11.

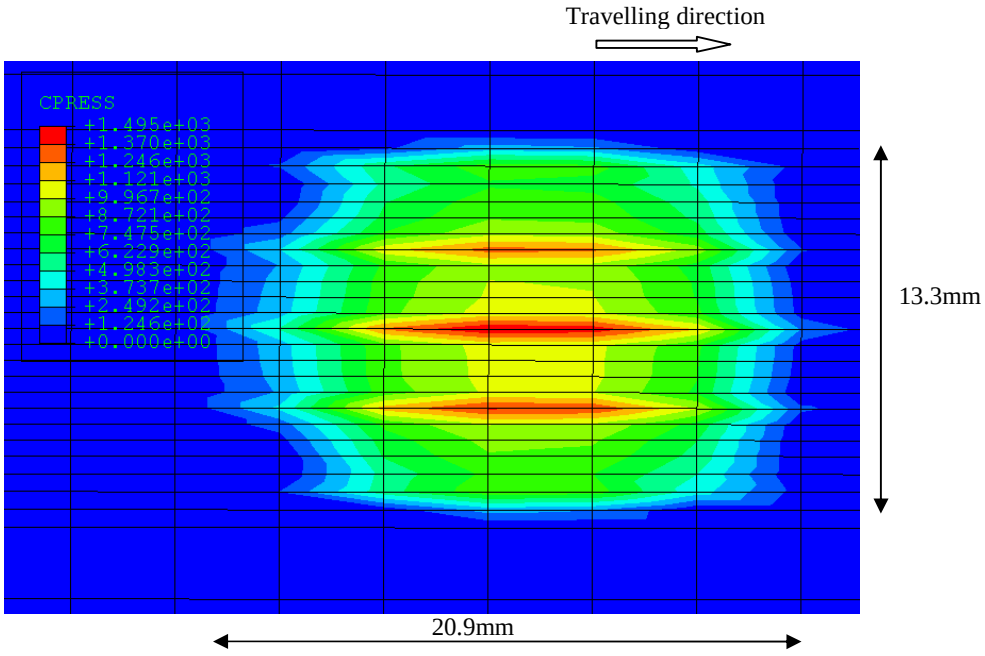


Figure 5.13 Contact pressure distribution (post impact)

The area of the contact patch obtained at each increment of the explicit analysis is plotted as a time history in Fig. 5.14. In this figure the contact area predicted by the HCT is also shown (as the horizontal straight line). Whilst the HCT predicts the area as 160 $mm^2$, the explicit dynamic analysis predicted areas varied around a value of approximately 260 $mm^2$ prior to impact, and has registered a sharp increase in the contact pressure area to 450 $mm^2$ at the time of impact, and 280 $mm^2$ post impact. The consistent deviation between HCT and FE results is primarily due to coarse mesh. Based on the discussion in Section 5.3.1, should the mesh be refined it is believed that the contact area pre and post impact would be fairly close to the HCT.

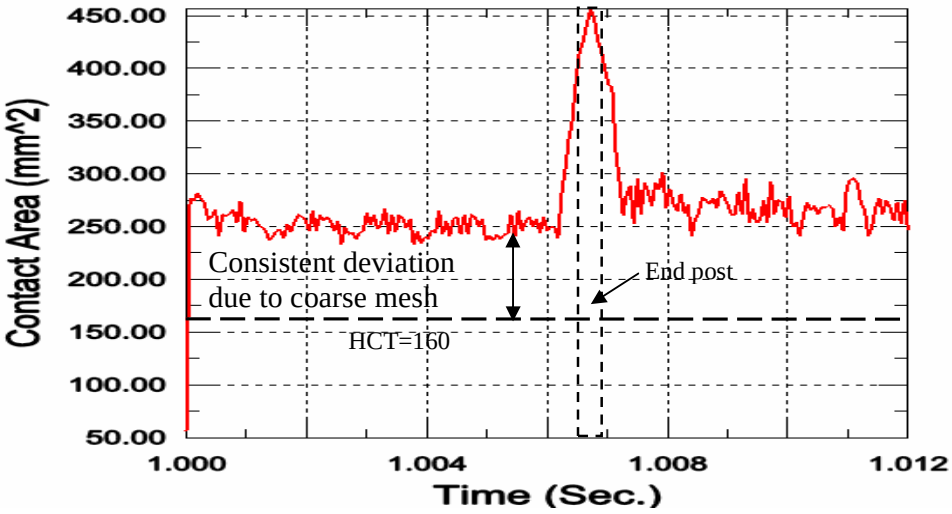


Figure 5.14 History of total area of contact

The time series of the maximum contact pressure is shown in Fig. 5.15. Except for the influence of the initial conditions, the contact peak pressure $P_0$ determined from the explicit FE analysis has exhibited reasonable agreement with that of the HCT analysis until the wheel was located approximately 20mm away from the edge of the rail and then started deviating from the HCT prediction at times of impact. Just after crossing the end post, $P_0$ has shown a steep raise to 1600MPa. The coarse mesh appear to have not affected the peak pressure significantly.

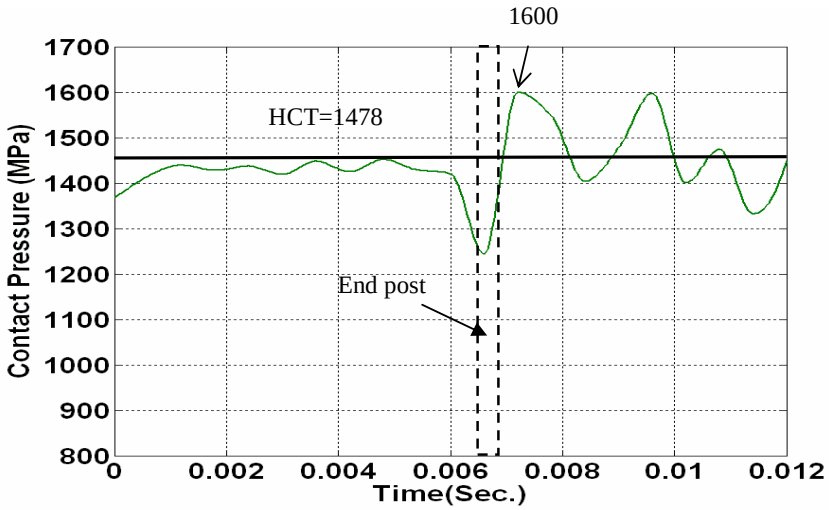


Figure 5.15 Time series of peak pressure $P_0$

**(c) Stresses**

The Von-Mises stress distribution presented in Fig. 5.16 shows the most part of the IRJ (excluding the contact patch of wheel and rail) is subjected stresses lower than 150 MPa (which will not cause any plastic deformation). The bolt pretension load has only a localised influence on the IRJ as shown in Fig. 5.16. The magnitude of Von-Mises stress in the bolt zone is also below 200MPa. Through these results, the assumption on the localised plastic zone of the IRJ used in the FE modelling is validated.

Prior to impact, the wheel/rail contact force remained at a stable level that produced a maximum Von Mises stress of 645MPa (the yield stress of steel was 780MPa). The maximum stress occurred at a point 3.75mm below the railhead surface shown in Fig. 5.17&5.18.

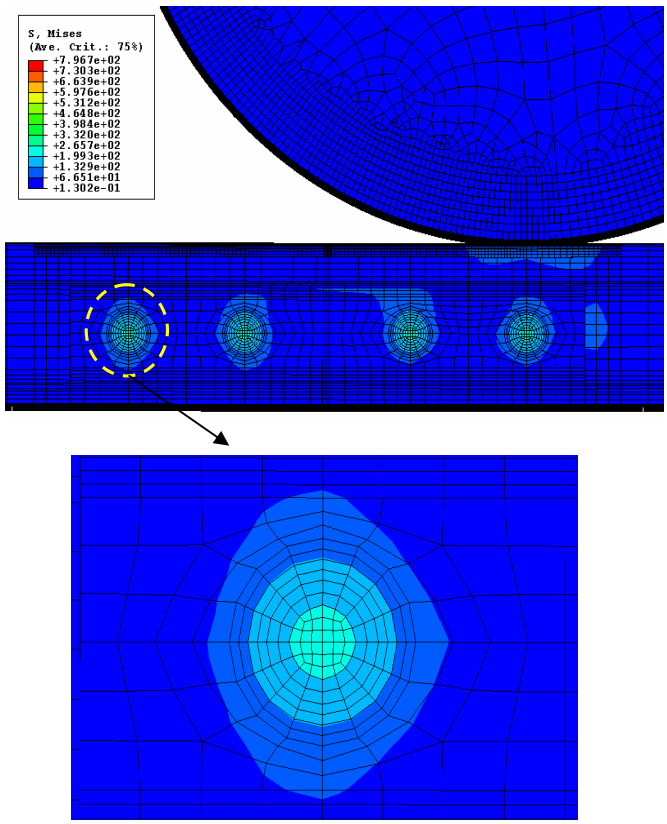


Figure 5.16 Von-Mises stress distribution

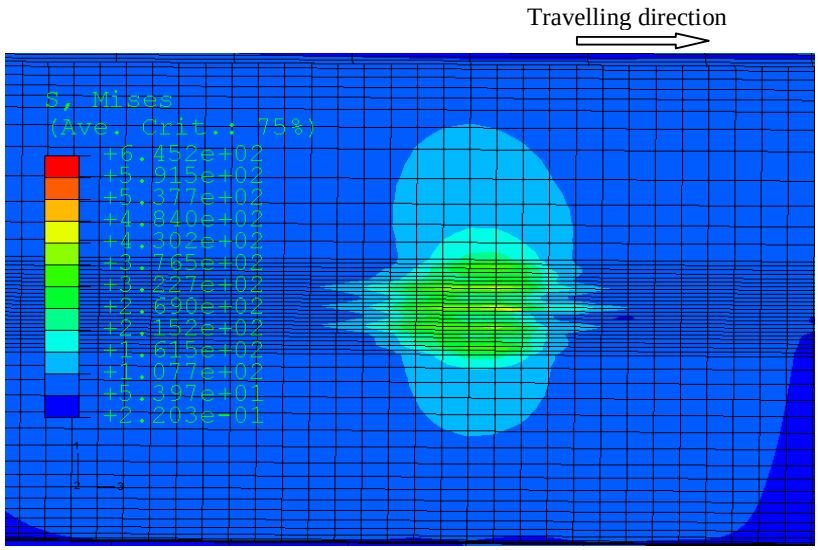


Figure 5.17 Von Mises stress contour (top of rail view) prior to impact

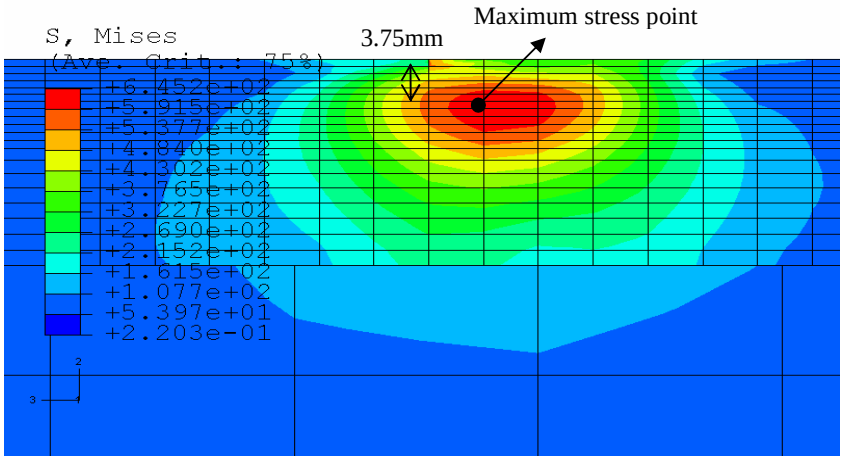


Figure 5.18 Von Mises stress contour (longitudinal vertical symmetric plane through the rail) prior to impact

At the time of impact, the contact force reached its maximum magnitude; the corresponding Von Mises stress distribution is shown in Figs. 5.19 & 5.20. The contours indicate that the Von Misses stress on the surface of the railhead was 668 MPa and the maximum stress of 798.7 MPa (greater than the rail material plastic stress) occurred at 3.19mm below the railhead surface. This shows the impact is the

major cause of the initiation of the damage near the edge of the rail in the vicinity of the end post.

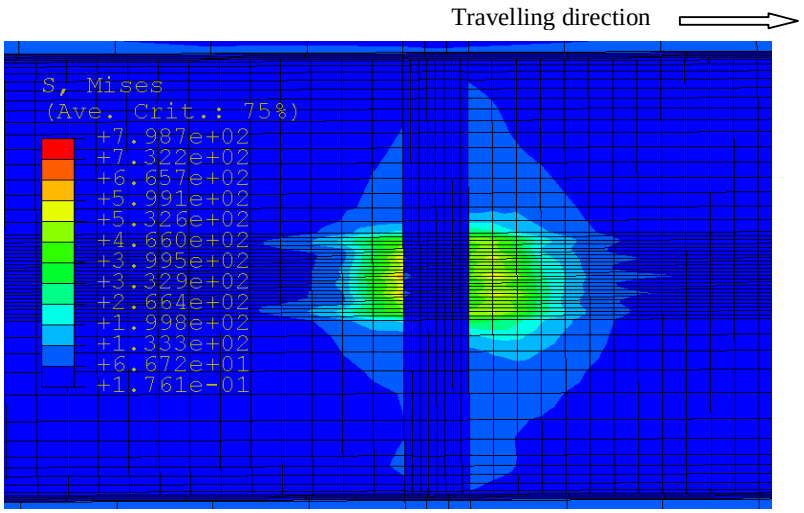


Figure 5.19 Von Mises stress contour (top of rail view) at impact

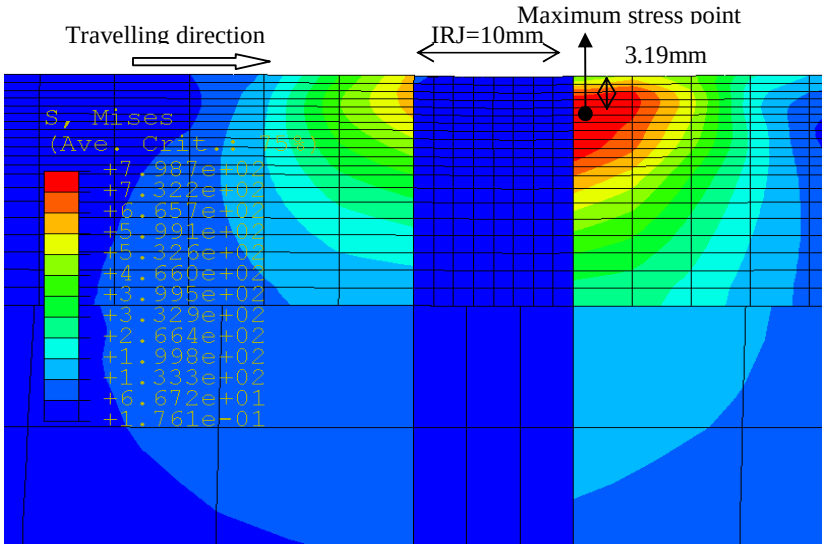


Figure 5.20 Von Mises stress contour (longitudinal vertical symmetric plane through the rail) at impact

The Von-Mises stress distribution post impact is shown in Fig. 5.21&5.22. The maximum stress is 736Mpa and located at 3.02mm beneath the railhead.

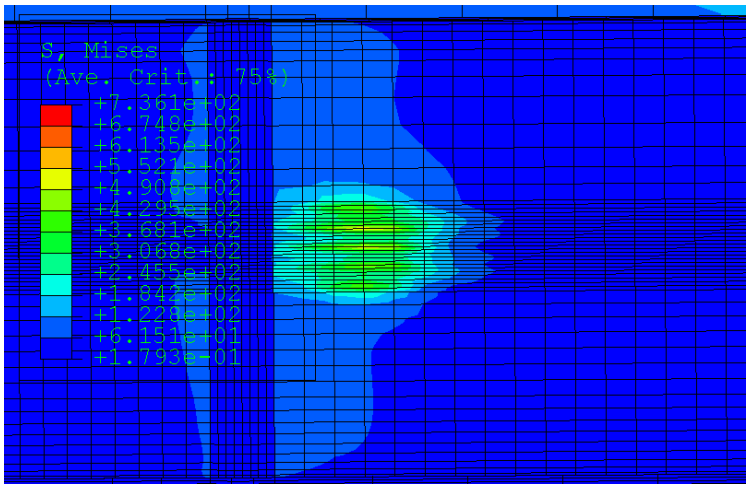


Figure 5.21 Von Mises stress contour (top of rail view) post impact

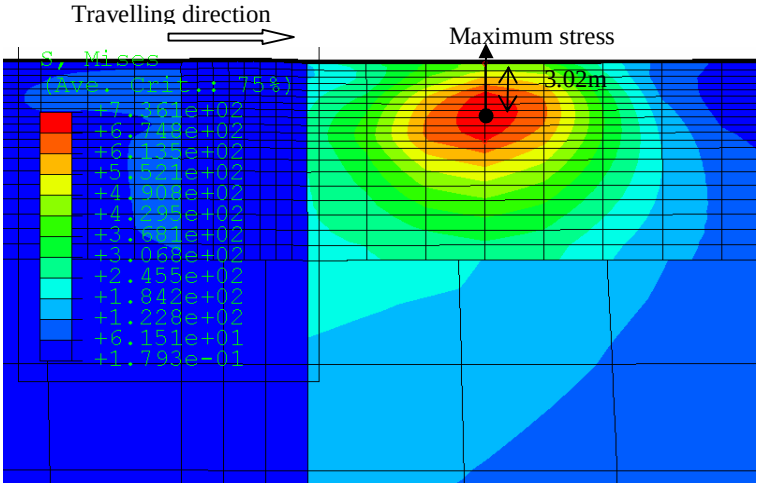


Figure 5.22 Von Mises stress contour post impact

Comparing the results of Von-Mises stress (Figs. 5.17 to 5.22) and contact pressure distribution (Figs.5.11 to 5.13), it appears that at impact, the peak contact pressure reduces (approx. 18.4% and 27.2% relative to pre-impact and post impact respectively) due to an apparent increase in contact area. In spite of the reduction in peak contact pressure, the maximum Von-Mises stress at impact is larger relative to the pre and post impact stages (approximately 21.2% and 12.5% respectively). Discontinuity of rail in the vicinity of the end post appears to be the primary factor influencing the large increase in Von-Mises stresses.

**(d) Energies**

In this section, kinetic energy ($\frac{1}{2}mv^2$) and plastic energy ($\frac{1}{2}\sigma\varepsilon_P$) time series are presented. The kinetic energy time series of the IRJ is plotted in Fig.5.23. The kinetic energy remained very high throughout the duration of wheel travel due to the significant contribution from the wagon mass which was 15 tonnes or 96% of the mass of the whole model. During the steady state rolling, the kinetic energy recorded a gradual reduction until the impact imparted higher levels of kinetic energy. The maximum peak of the kinetic energy occurred at 8.0 millisecond of travel time, which shows a delay of 0.9millisecond to the time of maximum impact force (Fig. 5.9). This time delay is in accordance to the theory of stress wave propagation in solids. When impact occurred, the stress waves propagated in the solids are reflected back as they reached boundaries. The reflected stress waves cause wheel response and propagated into the entire system. This whole process took some time and caused the time delay.

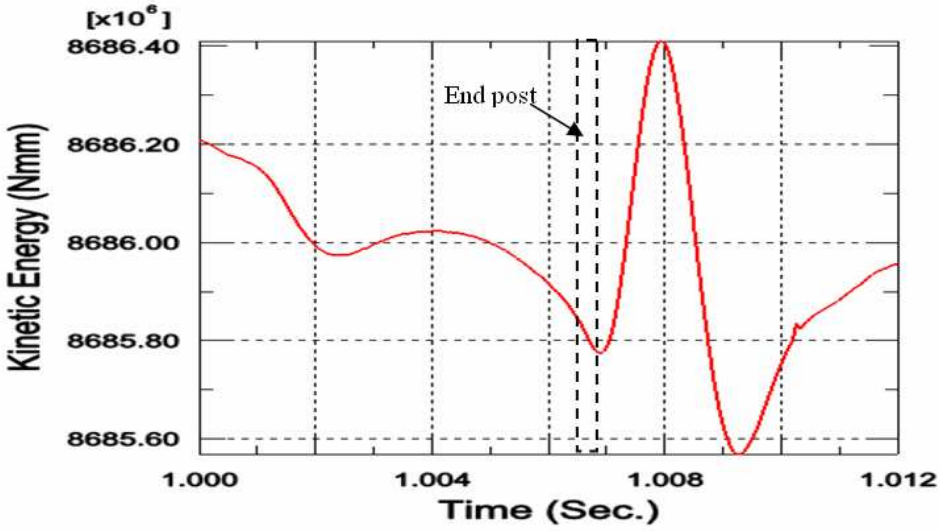


Figure 5.23 Kinetic energy time series

The Plastic energy history is plotted in Fig. 5.24. Impact has sharply increased the plastic strain energy to a higher value that gradually crept to a maximum steady state

level towards the end of the analysis. It has been found that the sharp increase of plastic energy occurred between 6.6ms and 7.1ms, corresponding to the impact (Fig. 5.9). This shows that the material is significantly plasticised due to wheel impact almost instantaneously.

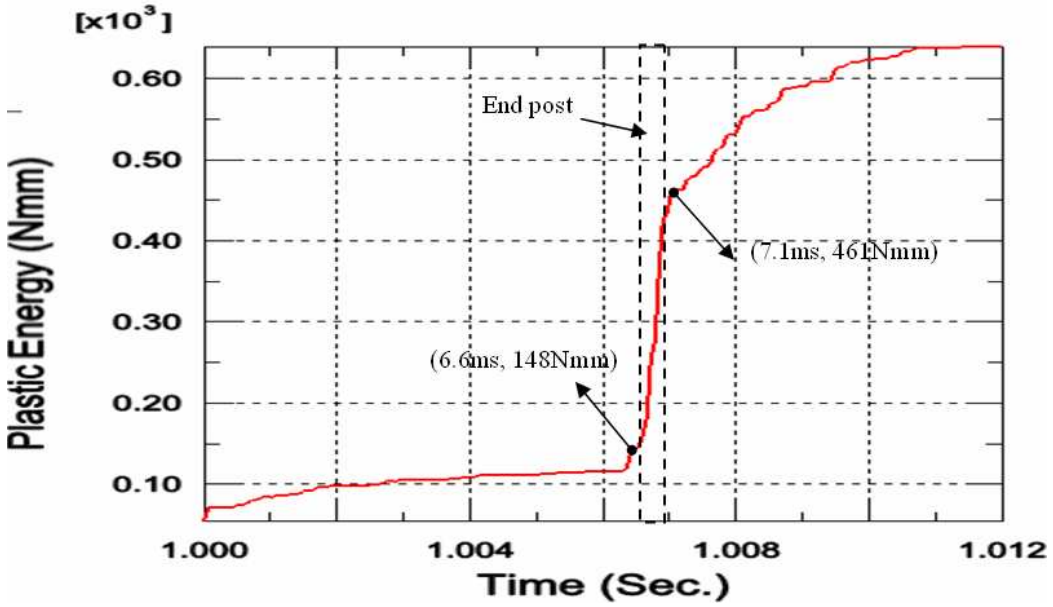


Figure 5.24 Plastic energy time series

Although the results presented so far illustrate the logical occurrence of impact in the vicinity of the end post, to further prove the appropriateness of the FE model for the contact-impact analysis, the end post material (nylon66) was replaced with the rail steel itself. This modification has effectively removed the joint (discontinuity), with the FE model of the IRJ becoming a rail with no joint; as such the model should predict no impact. The contact force time history shown in Fig. 5.25 proves that the FE model works well, as no impact is found with the contact force remaining at 150kN level (equivalent to static wheel load) throughout the travel and with the distinct absence of impact. The FE model is therefore regarded as being appropriate for the contact-impact study in this thesis. The model is further validated using some

limited experimental data as explained in Chapters 6 and 7. The FE model is then used to examine the sensitivity of the design parameters of the IRJ with a view to determining a low impact (or, optimal) design of IRJ.

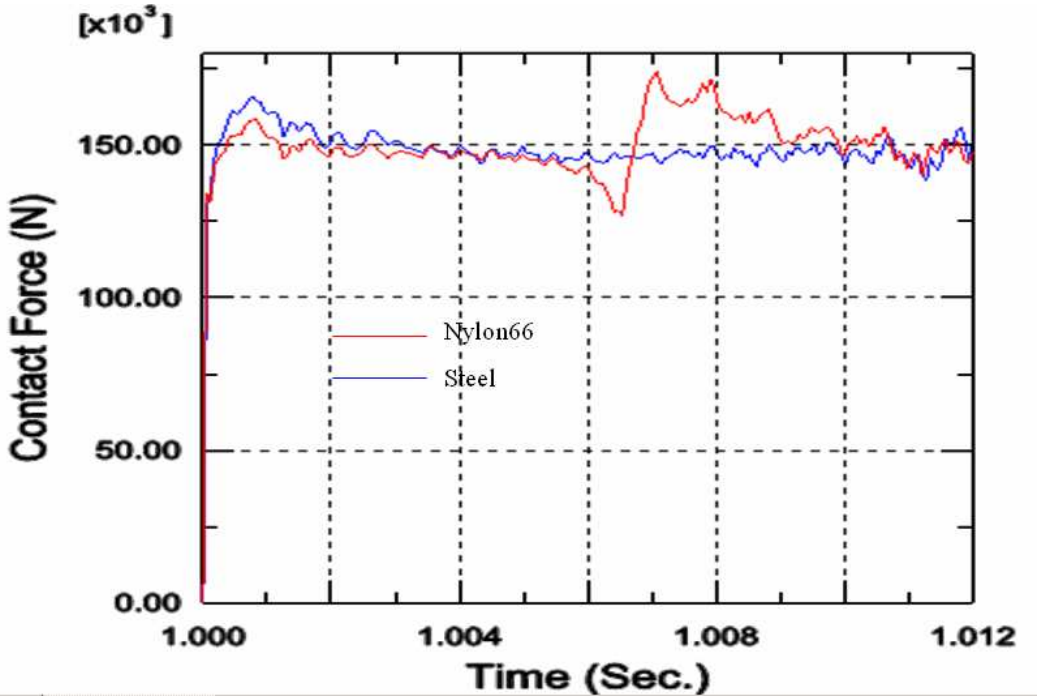


Figure 5.25 Contact force history of Nylon66 and Steel end post material

## 5.4. Sensitivity Analyses of Design Parameters of IRJ

There are a range of designs of IRJ available as discussed in Chapter 2. Sensitivity of a few major design parameters is reported. The basic design parameters examined are illustrated in Fig. 5.26; the sensitivity of these parameters to wheel/rail impact are reported in this section. The design parameters considered are:

(i.) End post bonding detail: glue or inserted

(ii.) Gap size: 5mm or 10mm

(iii.) Supporting system type: flexible or rigid

(iv.) Length of joint bar: 4 bolts or 6 bolts long

(v.) End post material: Nylon66, Fibreglass or Polytetrafluoroethylene (PTFE).

(vi.) Joint suspended or directly supported on sleeper

In addition to the above, an operational parameter, namely sliding of wheels across the joint was also considered and compared to the rolling case. In all analyses, other than the sliding analysis, the wheel was considered as undergoing pure rolling.

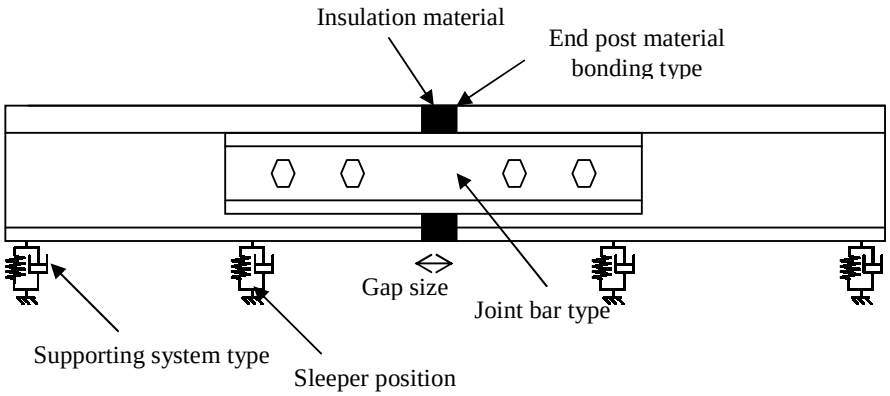


Figure 5.26 IRJ design parameters examined

### 5.4.1. Design cases considered

Each design case is uniquely identified by a combination of characters and/or numbers. The first character represents the end post bonding detail: **G** for glued and **I** for inserted (i.e. non-glue). The next two digits **05** or **10** represents the gap size 5mm or 10mm respectively. The fourth character, **F** or **R** is used for the flexible or rigid support at the base of the rail. The fifth and sixth characters stand for the length of joint bar, namely **4B** or **6B** standing for the 4-bolt joint bar or 6-bolt joint bar. The seventh character, **N**, **F** or **P** is used to specify the insulation material Nylon66, Fibreglass or PTFE respectively. The final three characters '**sus**'/ '**sup**' stand for

whether the joint is suspended between sleepers or directly supported on the sleeper. The design parameter sensitivity was inferred by comparing the results from one or two design cases with Case (1) that served as a base case as shown in Table 5.4.

Table 5.4 Sensitivity study plan

| Case Number | Sensitivity Studies | Explanation |
|---|---|---|
| (1) | **G10F4BNsus** | Base case |
| (2) | **I10F4BNsus** | Compare (2) to (1) for the determination of effectiveness of end post bonding detail |
| (3) | **G05F4BNsus** | Compare (3) to (1) for the determination of effectiveness of gap size |
| (4) | **G10R4BNsus** | Compare (4) to (1) for the determination of effectiveness of supporting system at rail base |
| (5) | **G10F6BNsus** | Compare (5) to (1) for the determination of effectiveness of length of joint bar |
| (6) | **G10F4BPsus** | Compare (6), (7) and (1) for the determination of effectiveness of type of end post material |
| (7) | **G10F4BFsus** | |
| (8) | **G10F4BNsup** | Compare (8) to (1) for the determination of effectiveness of suspended versus supported joint |

### 5.4.2. Sensitivity studies

In this section, the sensitivity of design parameters is reported by comparing the design cases discussed above. The wheel/IRJ contact-impact force, which is the key cause of IRJ failure, is chosen as the basis for sensitivity study.

Two types of wheel motion, namely pure rolling and pure sliding, are investigated first. Locked wheels due to heavy braking/ traction tend to slide and are known as the primary reason for “wheel burn” type damage even on rails with no joints. The FE model developed was used to analyse the effect of sliding wheels near the IRJ on the contact force history. The IRJ containing a glued end post was used for this purpose.

Degree of freedom 5 of the wheel was arrested to simulate dragged wheels. The contact force history shown in Fig. 5.27 illustrates the increase in impact force (194kN – 174kN = 20kN for a static wheel load of 150kN representing 13% increase) that is significant. It is, therefore, important the operating vehicles ensure good rolling of wheels through application of gentle braking/ traction torques.

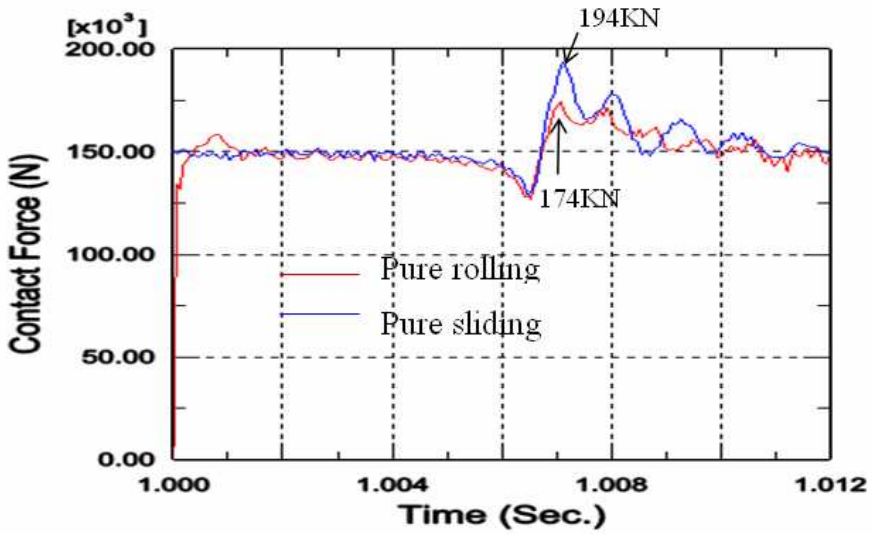


Figure 5.27 Contact force history of wheel pure rolling and pure sliding

## (a) Effect of end post material bonding detail

Fig 5.28 shows the modelling of the glued and inserted end post.

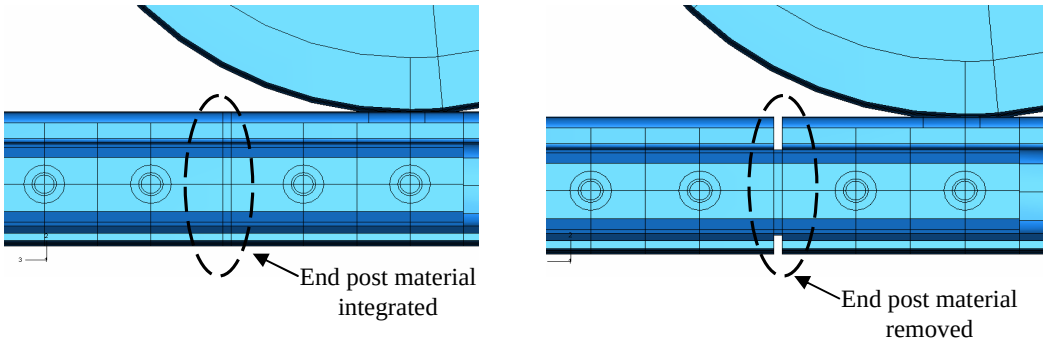


Figure 5.28 Modelling of end post material bonding detail

As the ‘inserted’ end post (non-glued) does not provide additional stiffness to the entire IRJ structure unlike the glued end post, it is generally expected that the ‘inserted’ type would generate higher impact. Modelling of the ‘inserted’ case of the end post is complex. To truly model this case, the end post surfaces and the rail end surfaces should all be initially defined as free. Progressively due to deformation, the model should account for the development of contact between these surfaces. For simplicity, the end post for the ‘inserted’ case was removed. Therefore it is expected that the model would predict high impact force as no benefit of partial support from the end post is accounted for in the model. The glued and inserted case modellings can therefore be regarded as lower and upper bound results.

Fig. 5.29 presents the contact-impact force histories of these two cases. The damage potential due to the increased impact of each wheel passage (185kN – 174kN = 11kN for a static wheel load of 150kN, or 8% increase) requires further investigation as the costs of gluing the end post against the potential increase in railhead damage requires economic justification. For the inserted (non-glued) case, the impact occurs 0.15ms later than for the glued case, corresponding to 48mm travel for the speed of 120Km/h. This suggests enlargement in the damage area of the IRJ.

### (b)Effect of gap size

The gap size of conventional IRJ designs normally range from 5mm to 10mm. In this sensitivity study, two sizes of gap (thickness of end post material) of 5mm and 10mm have been considered. The FE modelling was simply realised by partitioning the end

post zone for 5mm or 10mm, as shown in Fig. 5.30 for the two cases respectively.

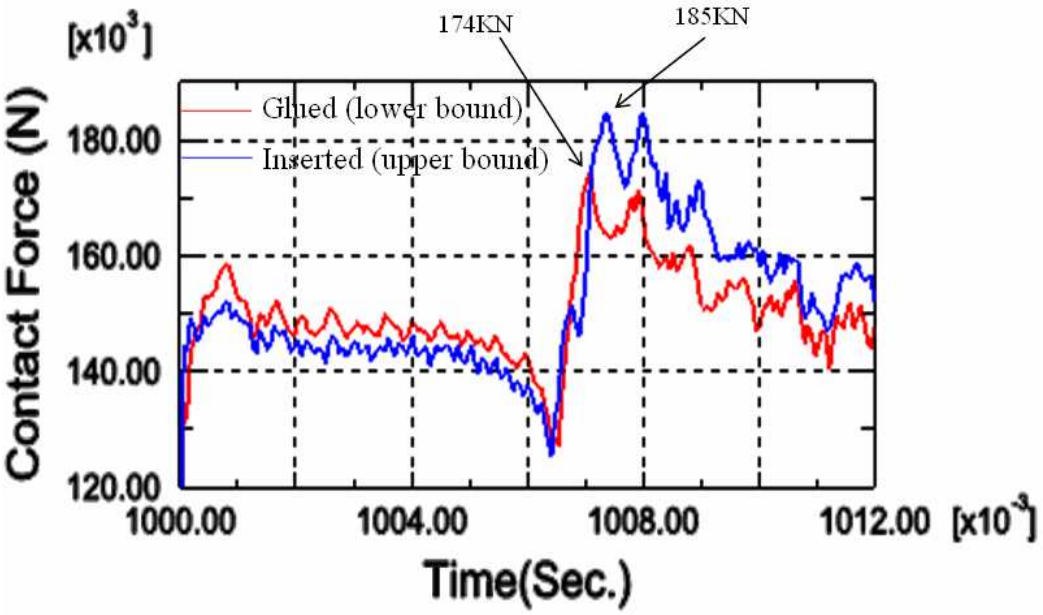


Figure 5.29 Contact force history of glued and inserted joint

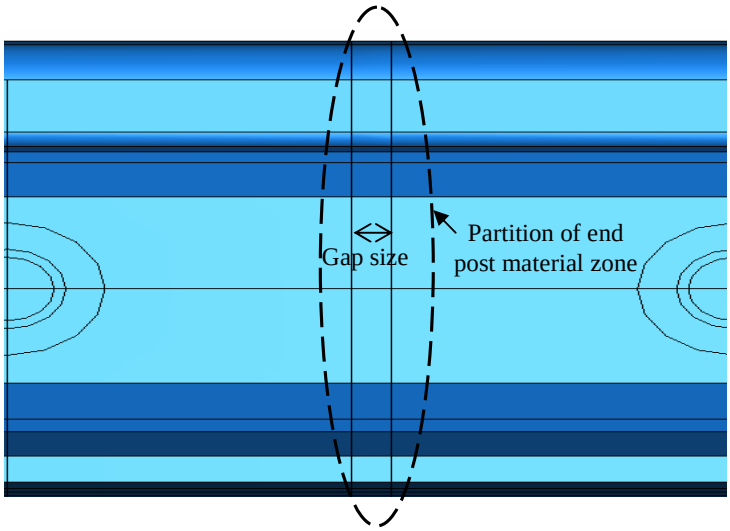


Figure 5.30 Modelling of gap size

The impact force time series for these two cases (cases (3) and (1)) are compared as shown in Fig. 5.31. The numerical result indicates that the small gap size reduces the

impact force by 11KN (174KN-163KN) or 7.3% of the static load of 150KN. Further economic and technical assessment is required as the thinner gap may increase the possibility of early electrical isolation failure.

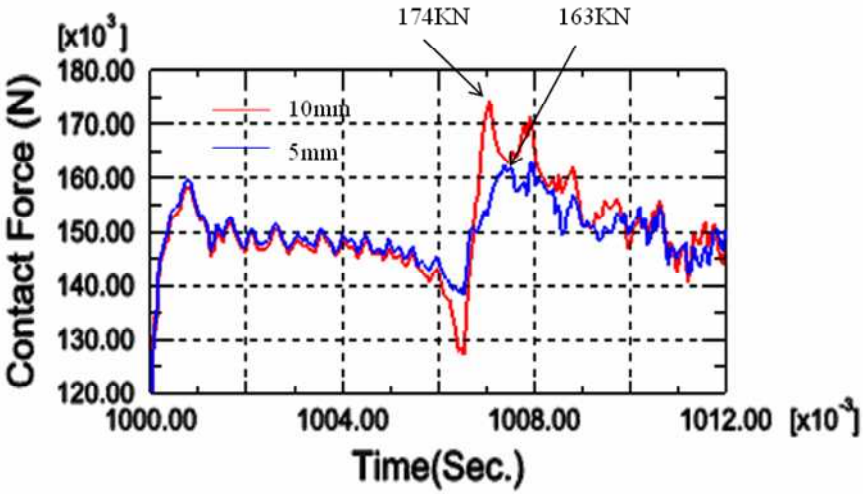


Figure 5.31 Contact force history of 10mm and 5mm gap size

### (c) Effect of support condition

The modelling of the rail support foundation has been studied by many researchers. Models using discrete spring/dashpot sets representing the supporting system are commonly adopted for railway track studies. However, the constants of springs and dashpots are varied depending on different practical conditions and models. To examine the effect of the spring constant, the supports beneath the rail base were either considered as either flexible or rigid, which is an extreme case for rigid springs. The flexible supporting system has been already introduced in the previous chapter. The rigid case is realised by removing the spring/dashpot sets and directly fixing the rail bottom to the ground at the positions of sleepers.

The result illustrates that without the damping effect of flexible springs, the impact force can reach as high as 205KN with an increase of 21KN over the flexible case or 14% of the static load of 150KN. Fig. 5.32 also infers that without foundation damping the wheel/rail contact exhibits more vibration and is slower to stabilise after impact.

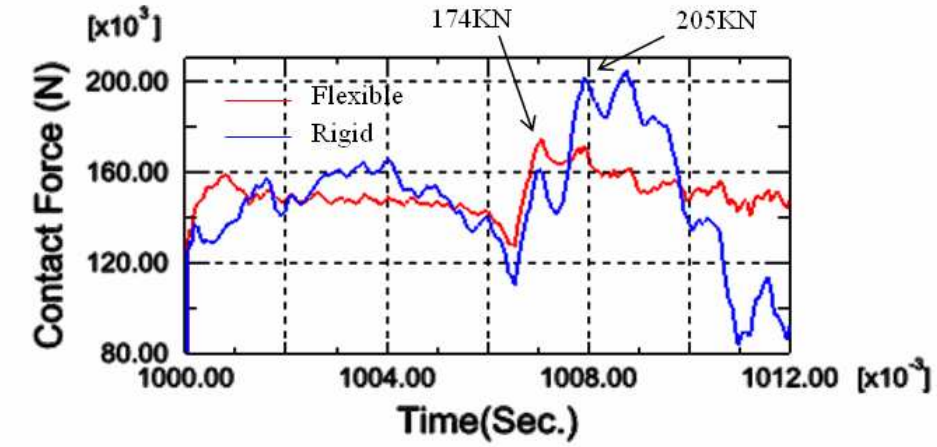


Figure 5.32 Contact force history of flexible and rigid support

## (d)Effect of joint bar length (number of bolts)

Two types, namely 4 bolt long and 6 bolt long joint bars as shown in Fig. 5.33 have been considered. The cross sections of these two joint bars were kept the same and the longitudinal lengths were 576mm and 830mm respectively.

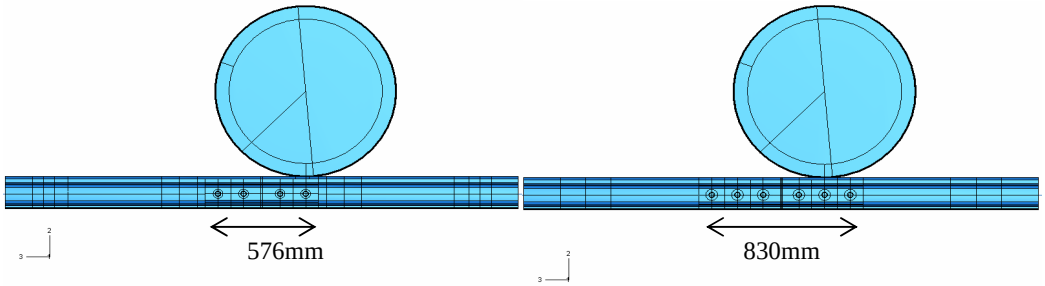


Figure 5.33 4-bolt and 6-bolt joint bar IRJ model

In this design case the 4-bolt joint bar is 254mm shorter than the 6-bolt joint bar in the longitudinal direction. As bolt pretension load is kept same, the four bolt joint bar has had lower pretension force in the lateral direction relative to the six bolt joint bar case. Fig. 5.34 illustrates that the 6-bolt joint bar IRJ generates a slightly larger impact force of 178KN compared to the 4-bolt joint bar case of 174KN. A conclusion can be drawn that the effect of the joint bar length and number of bolts on the impact force is not evident for reasons as explained below.

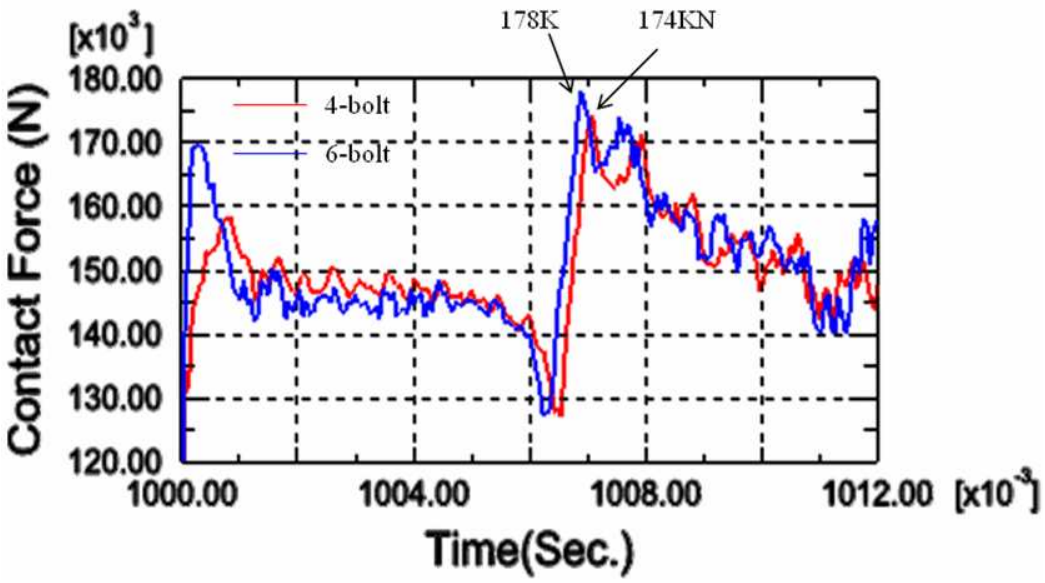


Figure 5.34 Contact force history of 4-bolt and 6-bolt joint bar

Considering the sleeper clear spacing is 564mm (Fig. 5.35), joint bars always span across sleepers whether 4-Bolts (576mm) or 6-Bolts (830mm) designs are used. Therefore their effect on impact is not significant in the cases considered. However, with 6-bolt joint bars, a larger sleeper spacing may be adopted. In the event of larger sleeper spacing, the 4-bolt case might generates larger impacts due to the larger dip (deflection) under wheel passage.

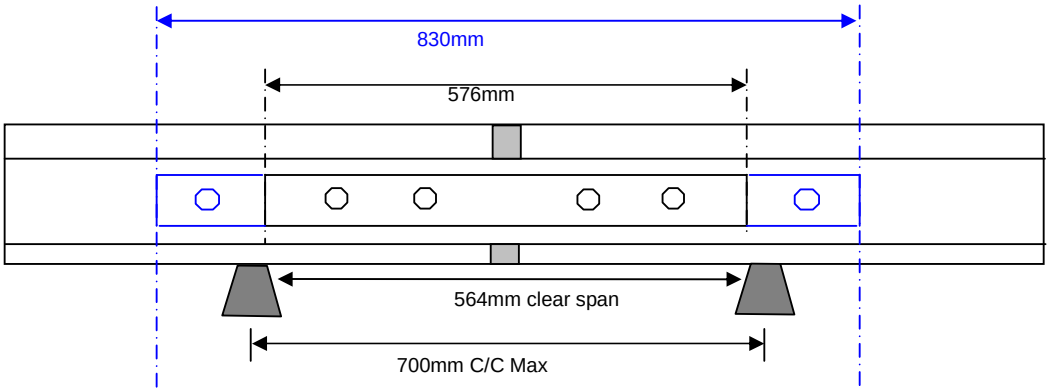


Figure 5.35 Illustration of sleeper spacing and joint bar length

### (e) Effect of end post material

Three insulation materials have been investigated in this study: Nylon66, PTFE and Fibreglass (case 1, 6 and 7). Table 5.5 shows the Fibreglass is the stiffest material and the PTFE is the softest of the three materials. The result of the study is presented in Fig 5.36, which shows that the IRJ with fibreglass exhibits the lowest impact force level of 168KN while the other two cases both reach 174KN. Although the peak impact forces are the same for Nylon66 and PTFE cases, the PTFE case shows more post impact vibration during the wheel passages and the peak value has occurred 1.2ms later than the other two cases, corresponding to 40mm length. This would mean that the damage area may larger for PTFE. In contrast, the fibreglass case shows not only a lower impact force but also less post impact vibration.

Table 5.5 Mechanical properties of insulation material (Chen, 2002)

| | PTFE | Nylon66 | Fibreglass |
|---|---|---|---|
| Young's modulus $E$ | 400MPa | 1590MPa | 45000MPa |
| Poisson's ratio $\nu$ | 0.46 | 0.39 | 0.19 |

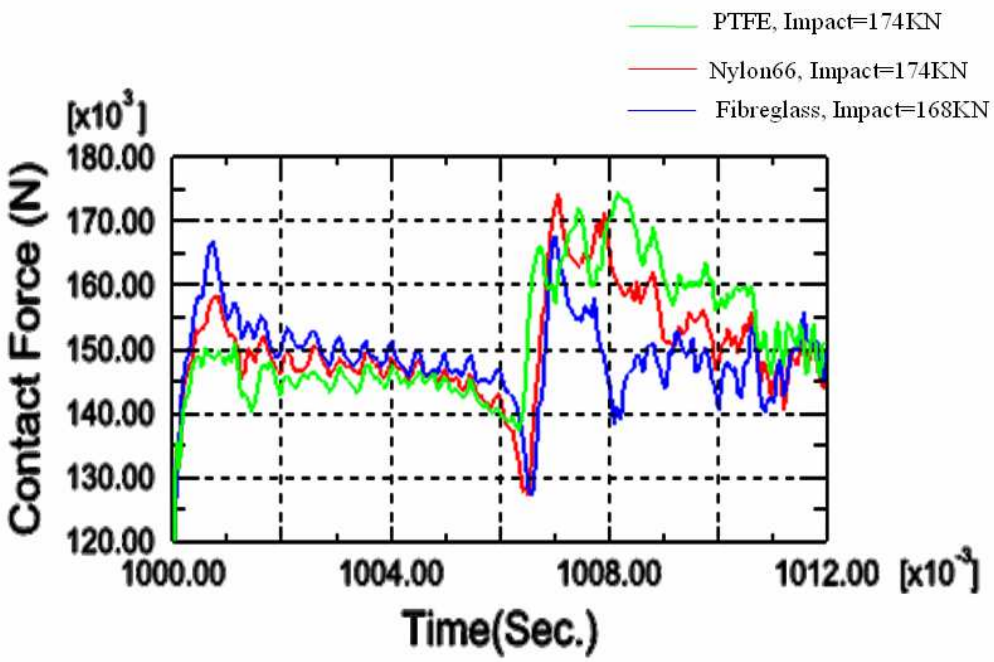


Figure 5.36 Contact force history of different end post material

## (f) Effect of sleeper position

The sleeper position effects on the wheel/rail contact impact at the IRJ were studied by positioning the end post either symmetric to the sleepers (suspended IRJ) or directly on the sleeper (supported IRJ). Fig. 5.37 shows these two cases (case 1 and 8 respectively). The sleeper spacing was kept the same for both cases.

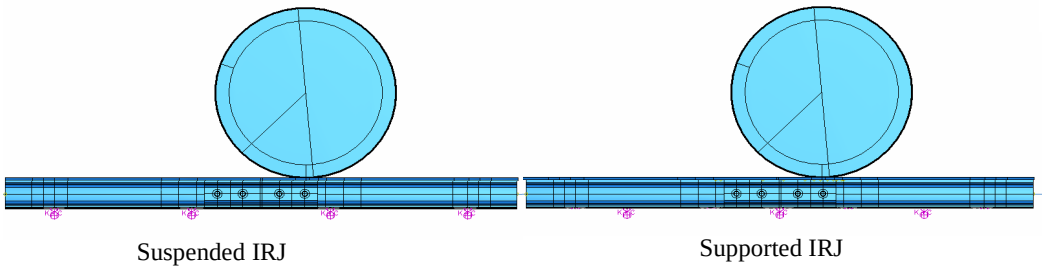


Figure 5.37 Position of sleepers

Fig. 5.38 shows that the supported IRJ has generated an impact force of 192KN, while the suspended IRJ has generated just 174KN impact force. The impact force difference is almost 12% of the static load of 150KN. The supported IRJ also exhibited significant post impact vibration. A similar response was also exhibited for the case of rigid support (Fig. 5.32). This shows that when either the support is stiffer or the IRJ is directly supported, the waves generated due to impact reflect more strongly resulting in the post vibration effect lasting longer.

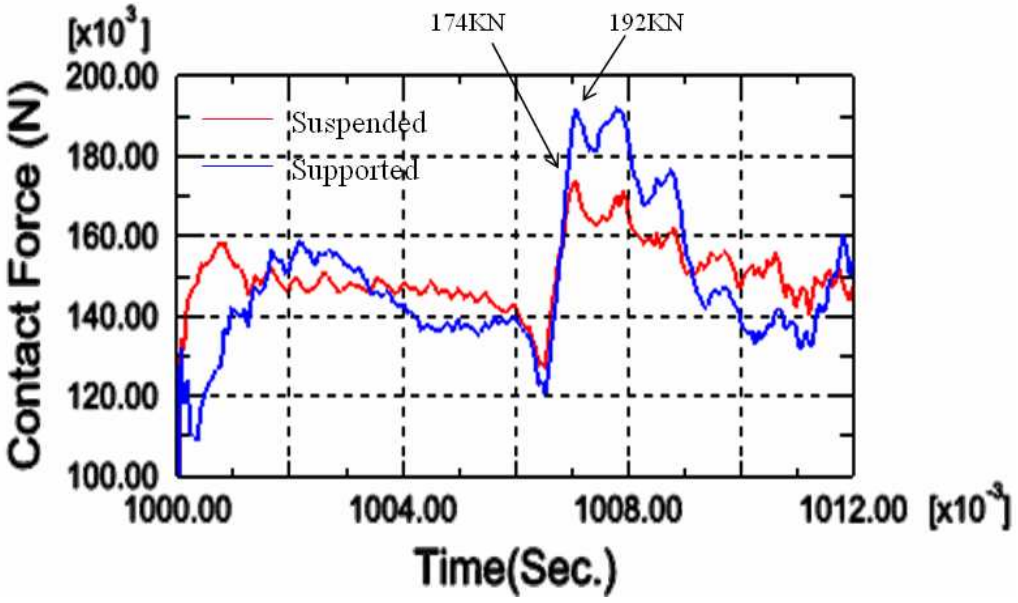


Figure 5.38 Contact force history of IRJs suspended or supported

### 5.4.3. Discussion of sensitivity study results

Through the analyses of these eight design cases, the effects of the selected design parameters on the wheel/rail contact-impact forces are investigated and a few conclusions are drawn.

- The glued IRJ performs better than the inserted (non-glued) IRJ. The IRJ with a smaller gap size generates less impact.
- The higher the flexibility of the supporting system, the lower the wheel/rail contact-impact.
- The effects of joint bar length seem to not be significant to the wheel/rail impact force based on the numerical results. Both the 4-bolt joint bar and the 6-bolt joint bar have just enough length to span across the clear spacing of the sleepers. Should the sleeper spacing be larger than the 4 bolt joint bar length, the result would have been different.
- The stiffer the end post material (fibreglass in this case), the lower the impact forces. This is because the material with mechanical properties closer to steel decreases the discontinuity in stiffness in the vicinity of the end post.
- It seems not a good choice to place a sleeper directly underneath the IRJ end post. The directly supported IRJ generates much larger impact forces relative to the suspended IRJ.

In summary, to minimise the wheel/rail contact impact force at the IRJ, the best design parameter combination is a fibreglass end post with 5mm gap size that is glued to the rail sections suspended between the flexible supporting system (**G05F4BFsus**). Fig. 5.39 indicates that the impact force is largely eliminated in this case. From a practical perspective, this case may be considered technically optimal.

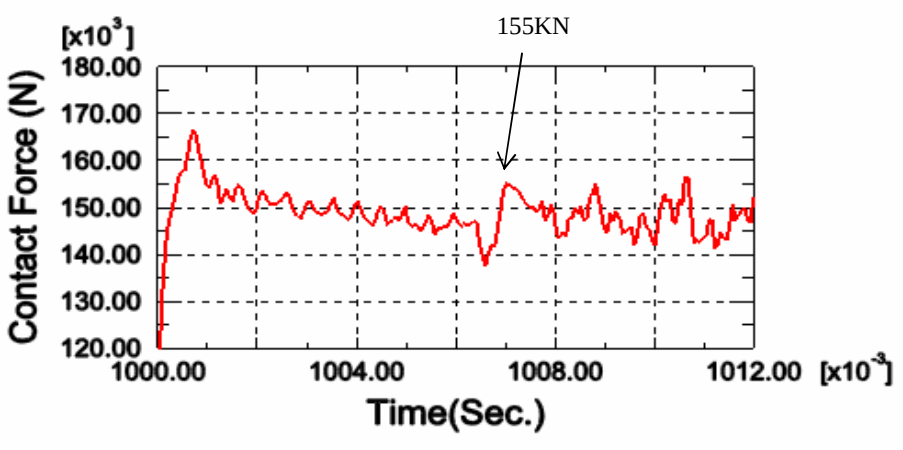


Figure 5.39 Contact force history for case **G05F4BFsus**

## 5.5. Summary

The wheel/rail contact impact at IRJs has been studied and reported in this chapter. The wheel/rail contact force history indicates that the impact is generated due to a 'two-point contact' as the wheel passes over the joint due to a flexible deformation of the joints in the vicinity of the end post. This flexibility causes an early reduction in the contact force below the static wheel load. At the time of impact, the wheel lands on the end of the rail on the other side of the joint, with the impacting point several millimetres away from the rail end and whilst the first rail end is still in contact with the wheel. It is notable that the structural deformation of IRJs during the impact is recoverable, although some plastic deformation may have occurred at the rail head. The impact mechanism can be explained as one caused by the IRJ stiffness discontinuity leading to the temporary geometry discontinuity under wheel passages as:

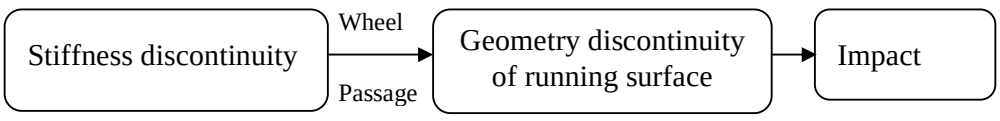

It has been shown that the contact pressure distribution, in particular the contact patch dimensions and the contact area, are significantly affected by the mesh size. Due to the limitation of the computational facility, the mesh was made coarse. It was found that, in the dynamic analysis although the contact area was consistently larger than HCT, the peak contact pressure was not affected indicating mesh changes to the distribution of pressure within the contact patch.

The HCT is proved valid as long as the wheel/rail contact area remains away from the joint. Dynamic results indicate that the Hertz contact theory is not strictly valid due to edge effect and material plasticity during the occurrence of impact.